Physica B 474 (2015) 97–104

Contents lists available at ScienceDirect

Physica B

journal homepage: www.elsevier.com/locate/physb

Microstructure, electronic structure and optical properties of combustion synthesized Co doped ZnO nanoparticles

N. Srinatha [a], K.G.M. Nair [b], Basavaraj Angadi [a,*]

[a] Department of Physics, JB Campus, Bangalore University, Bangalore 560056, India
[b] UGC-DAE-CSR, Kalpakkam Node, Kalpakkam, Kokilamedu 603102, India

ARTICLE INFO

Article history:
Received 11 March 2015
Received in revised form
31 May 2015
Accepted 11 June 2015
Available online 14 June 2015

Keywords:
ZnO
L-Valine
Atomic multiplet calculations
Electronic structure
Diffuse reflectance
Photoluminiscence

ABSTRACT

We report on the microstructure, electronic structure and optical properties of nanocrystalline $Zn_{1-x}Co_xO$ (x=0, 0.01, 0.03, 0.05 and 0.07) particles prepared by solution combustion technique using L-Valine as fuel. The detailed structural and micro-structural studies were carried out by XRD, HRTEM and TEM-SAED respectively, which confirms the formation of single phased, nano-sized particles. The electronic structure was determined through NEXAFS and atomic multiplet calculations/simulations performed for various symmetries and valence states of 'Co' to determine the valance state, symmetry and crystal field splitting. The correlations between the experimental NEXAFS spectra and atomic multiplet simulations, confirms that, 'Co' present is in the 2+ valence state and substituted at the 'Zn' site in tetrahedral symmetry with crystal field splitting, $10Dq = -0.6$ eV. The optical properties and 'Co' induced defect formation of as-synthesized materials were examined by using diffuse reflectance and Photoluminescence spectroscopy, respectively. Red-shift of band gap energy (E_g) was observed in $Zn_{1-x}Co_xO$ samples due to Co (0.58 Å) substitution at Zn (0.60 Å) site of the host ZnO. Also, in PL spectra, a prominent pre-edge peak corresponds to ultraviolet (UV) emission around 360–370 nm was observed with Co concentration along with near band edge emission (NBE) of the wide band gap ZnO and all samples show emission in the blue region.

1. Introduction

ZnO, is a II–VI semiconductor, with wide band gap of 3.37 eV and having a large exciton binding energy (60 meV) [1]. Due to its extra-ordinary properties, it is considered to be a most promising candidate for many potential applications, such as electronic, opto-electronics [2] and as a dilute magnetic semiconductor (DMS) for spintronics [3]. Currently, much emphasis has been given on the experimental and theoretical prediction of room temperature ferromagnetism (RTFM) in transition metal doped ZnO [4–5]. It has been reported that, the existence of RTFM in DMS's is sensitive to the preparation methods and preparation conditions. There are reports of synthesis of RTFM DMS materials by various methods, including sol–gel, co-precipitation, spray pyrolysis, solution combustion [6], etc. Among all the conventional methods, solution combustion technique (SCT) has greater advantages, as it produce fine, large surface area and sinter-active particles by using different precursors and the fuels [6]. Among all the transition metal doped ZnO based DMS's Co doped ZnO based DMS materials are of great interest, due to the tunability of FM above RT, high solubility limit and large magnetic moment per 'Co' ion [7–10]. But achieving single-phase is relatively difficult due to the formation of 'Co' metallic clusters or other impurity oxide phases. In addition, the detection of possible presence of small amount of impurities which contributes to the net magnetisation is indeed important for understanding the origin of ferromagnetism. That is, through the investigation of the electronic structure of the impurity ions in host material would help us to understand the local environment around the 'Co' in the host matrix which is responsible for the net magnetism of the sample. On the other hand, transition metal ion doped ZnO (for DMS) provides a possibility of tuning band gap energy by varying the concentration of the impurity ions in the host material. In other words, controlled doping of ZnO with transition metals offers a viable means of tuning the band gap [11]. Hence, a linear variation in the band gap with composition is expected. It is reported in the literature [12] that the band gap of Co doped ZnO increases with increase in 'Co' concentration and this blue shift was explained on the basis of Moss–Burstein effect [13]. Also, Kim et al. [14] reported that Co doped ZnO thin films show a decrease in band gap with increase in Co concentration and a similar behavior was reported by Bouloudenine et al. [15] in polycrystalline samples prepared by hydrothermal method. This red

* Corresponding author.
E-mail address: brangadi@gmail.com (B. Angadi).

http://dx.doi.org/10.1016/j.physb.2015.06.009
0921-4526/

shift is mainly due to the sp–d exchange interactions between the band electrons and the localized d electrons of 'Co' ions substituting Zn ions [17]. However, combined study of an electronic structure (indirect evidence to the net magnetism) and semiconducting (optical) properties, that is the variation of band gap energy and defect induced luminescence are indeed required for understanding the effect of doping on the semiconducting properties as well as the electronic structure for practical applications in spintronics. Hence, in the present work, we synthesized and studied the structural, micro-structural, optical properties and also report an electronic structure of Co doped ZnO nanocrystalline particles synthesized by solution combustion technique.

2. Experimental

Nanocrystalline $Zn_{1-x}Co_xO$ (x=0, 0.01, 0.03, 0.05 and 0.07) particles were prepared by the SCT using Zinc Nitrate Hexa-hydrate as an oxidizer and L-Valine as a fuel and Cobaltous Nitrate Hexa-hydrate as dopant. The stoichiometric balanced equation used for the synthesis of Co doped ZnO samples as follows:-

$$27(1-x)Zn(NO_3)_2{\cdot}6H_2O + 27xCo(NO_3)_2{\cdot}6H_2O + 10C_5H_{11}NO_2 \rightarrow 27Zn_{1-x}Co_xO + 50CO_2 + 32N_2 + 217H_2O$$

The stoichiometric amounts of precursors were taken based on the condition that the valances of O/F ratio to be unity, using total oxidizing and reducing valences of the precursors. These stoichiometric amounts of precursors were dissolved in double distilled water and stirred completely to get transparent solution. The transparent solution was dried in muffle furnace at 100 °C to remove water content in the solution. So obtained sticky solution (water free) was then placed in the pre-heated muffle furnace at 400 °C. Within a 5 min, the solution (gel) ignites, fires with flame and finally left with voluminous foamy product (ash). The final foamy product was collected and ground using agate make pestle and mortar.

As-synthesized samples were characterized for phase purity using X-Ray Diffractometer (D8 ADVANCE, Bruker) with wavelength 1.5418 Å. Rietveld refinement has been carried out using Fullprof software [16], to understand the structure of as-synthesized $Zn_{1-x}Co_xO$ samples. The detailed micro-structural and structural studies were carried out for the as-synthesized ZnO samples through High Resolution Transmission Electron Microscopy (HR-TEM) using LIBRA 200 TEM (M/s Carl Zeiss, Germany). The electronic structure was investigated through NEXAFS. The atomic multiplet calculations were carried out using the CTM4XAS software and the resultant spectra were compared with the experimental NEXAFS spectra. X-ray absorption spectroscopy (XAS) i.e., NEXAFS measurements were carried out at different beamlines (BL-11A, 17C and 20A) available at National Synchrotron Radiation Research Center (NSRRC) in Taiwan. All the beamline X-ray absorption data was obtained in the fluorescence yield (FLY) mode, which is mostly bulk sensitive. Room temperature diffused reflectance spectra were recorded in the 200–1600 nm wavelength range using a DRS Spectroscopy Model: JASCO V 670, Japan. The Photoluminescence spectra were recorded in the wavelength range from 350 to 600 nm with excitation wavelength of 325 nm.

3. Results and discussions

3.1 Structural analysis by XRD

Rietveld fitted XRD patterns of $Zn_{1-x}Co_xO$ (x=0, 0.01, 0.03, 0.05 and 0.07) samples are depicted in Fig. 1. From Fig. 1, it is observed

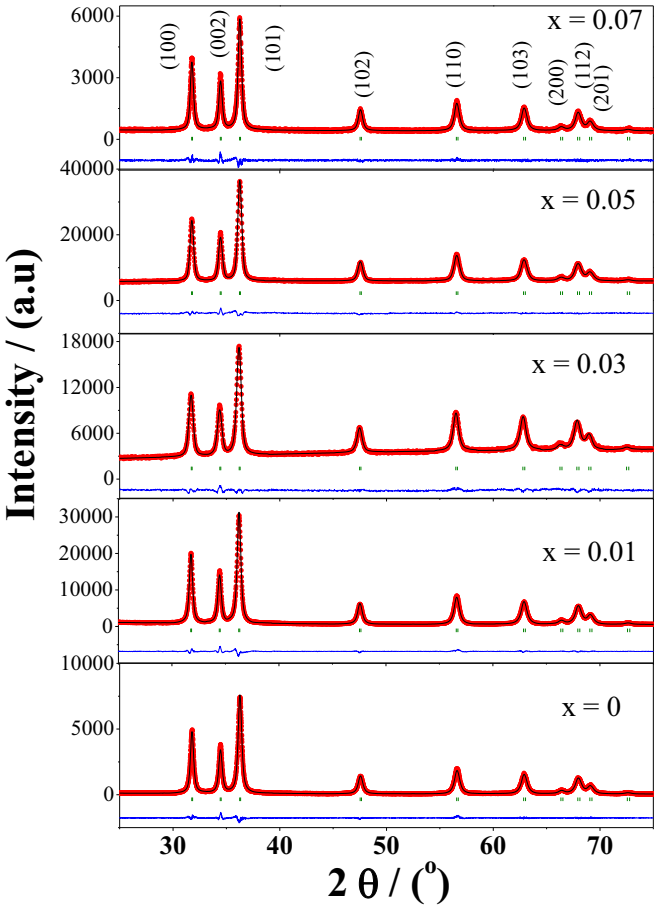

Fig. 1. Rietveld fitted XRD pattern of $Zn_{1-x}Co_xO$ (x=0, 0.01, 0.03, 0.04 and 0.05) samples.

that, all reflections/peaks are fitted well and all reflections are indexed to JCPDS card no. 36-1451 belongs to hexagonal wurtzite ZnO phase with space group *P63mc*. Also, confirms the formation of single-phase, polycrystalline in nature and no secondary/impurity phase like, CoO_x, metallic Co, etc is observed. It confirms that, 'Co' ions are substituting 'Zn' ions without any secondary phase formation. The estimated lattice parameters from the Rietveld refinement on XRD data were discussed in our earlier work [17]. Crystallite size and strain are calculated using Williamson–Hall equation [18].

$$\beta\cos\theta = \frac{k\lambda}{D} + 4\varepsilon\sin\theta \quad (1)$$

where, β is the observed FWHM, θ is the Bragg angle, k is the Scherer's constant, λ is the wavelength of the X-ray used, D is the crystallite size, ε is the strain present in the crystal. From the plot of $\beta\cos\theta$ along the y-axis and $4\sin\theta$ along the x-axis, the slope gives strain (ε) and the intercept gives $\left(\frac{\lambda k}{D}\right)$, from which crystallite size was calculated. The average crystallite size found to be in the range between 20 and 30 nm. The estimated values of crystallite size and strain are shown elsewhere [17].

3.2 Microstructural studies by TEM

The Transmission Electron Microscopy (TEM) micrographs of pure ZnO and $Zn_{0.99}Co_{0.01}O$ are depicted in Fig. 2. TEM micrographs, Fig. 2(a) and (c), shows the distribution of particles and their corresponding histogram (insets) of pure ZnO and $Zn_{0.99}Co_{0.01}O$, respectively and Fig. 2(b) and (d) represents their

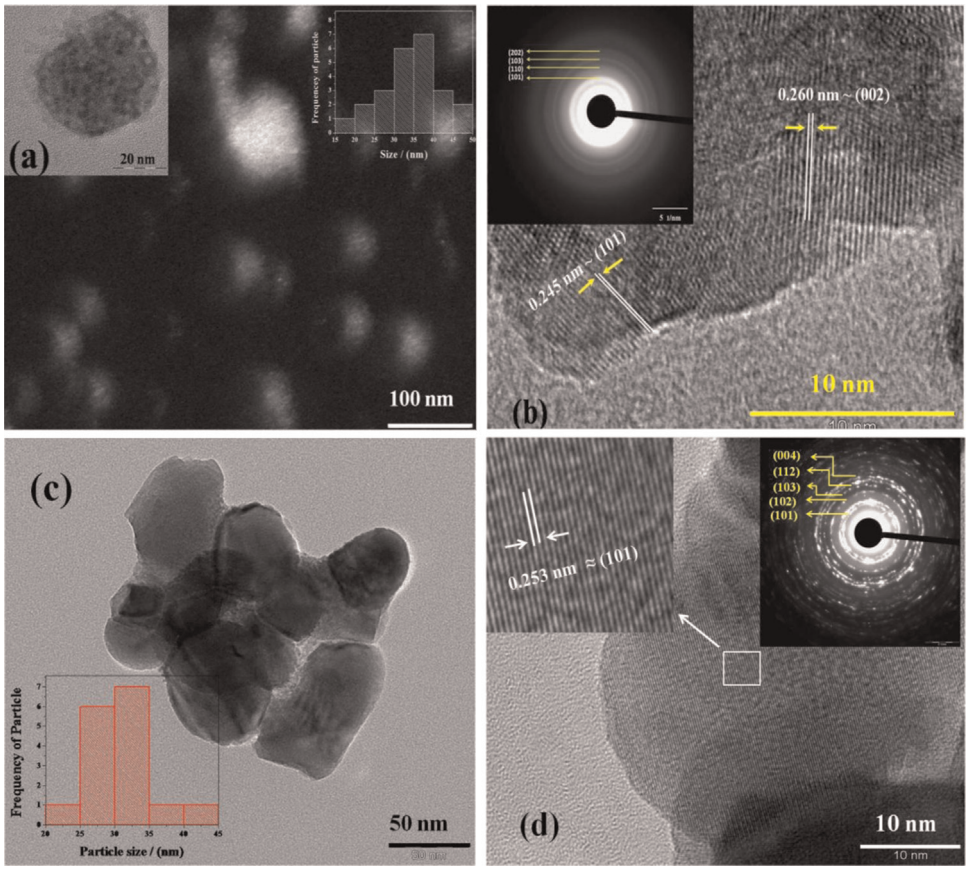

Fig. 2. TEM micrographs of pure and $Zn_{0.99}Co_{0.01}O$ nanoparticles. (a) TEM micrograph of pure ZnO taken with the dark field imaging whereas (b) is for $Zn_{0.99}Co_{0.01}O$ samples, insets shows their corresponding histogram of particle size distribution and (b and d) HRTEM, inset shows SAED pattern of pure ZnO (a and b) and for $Zn_{0.99}Co_{0.01}O$ (c and d) samples, respectively.

corresponding HR-TEM image and the insets shows SAED patterns. Fig. 2(a) shows the TEM micrograph taken with dark field imaging, left inset shows the single particle and right inset is the particle distribution. It is found from the TEM micrographs that, the particles are agglomerated, having wide distribution ranging from 15 to 50 nm for pure ZnO and 30–45 nm for $Zn_{0.99}Co_{0.01}O$. The average particle sizes estimated from the TEM micrographs are found to be 33 nm and 31 nm for pure ZnO and $Zn_{0.99}Co_{0.01}O$, respectively. These values are in agreement with those obtained from XRD and SEM measurements. Few particles appear to be larger in size, due to the aggregation of smaller particles due to the evolution of large amount of gaseous products during combustion. Also from HRTEM image, the fringe width (d-spacing) is determined. In case of pure ZnO, the d-spacing values are found to be 0.260 nm∼(002) and 0.245 nm∼(101). The (002) and (101) planes were assigned after comparing the measured d-spacing values with those from the standard JCPDS pattern (# 36-1451). This indicates that, the particles are having orientations along (002) and (101) planes, whereas, in case of $Zn_{0.99}Co_{0.01}O$, the d-spacing value found to be 0.253 nm for (101) plane. The corresponding SAED patterns are shown as inset in Fig. 2(b and d). The SAED shows clear ring patterns, indicating the polycrystalline nature of the sample. All the ring patterns were indexed to the JCPDS pattern # 36-1451, confirming the formation of ZnO wurtzite nano structure.

Further, lattice parameters were estimated using TEM-SAED patterns. The Bragg angle (2θ) was determined from the interplanar d-spacing which was obtained from SAED patterns using the formula, $n\lambda = 2d\mathrm{Sin}\theta$. The lattice parameters were estimated through unit cell program [19] having known ($h\ k\ l$) and 2θ values. The estimated lattice parameters for pure ZnO are '$a=b=3.328$ Å and $c=5.298$ Å' and for $Zn_{0.99}Co_{0.01}O$ are '$a=b=3.251$ Å and $c=5.119$ Å'. It is observed that, the estimated lattice parameters from TEM-SAED patterns are in agreement with those obtained from Rietveld refinement.

3.3 Electronic structure

Substitution of 'Co' at 'Zn' site in the host alters the local environment around it depending on its valence state, which reflects as features in the NEXAFS spectra. The NEXAFS is an element specific technique and is very sensitive to the bonding environment of the absorbing atom. In other words, it is the fingerprint technique to determine the valance state of 'Co' ion and its substitution at 'Zn' site in the host ZnO. It also helps to determine the possibility of existence of 'Co' ion as clusters or in any other oxide phase. The NEXAFS spectra of Co doped ZnO taken at Co L3,2-edge is depicted in Fig. 3. The results of NEXAFS along with XMCD have been reported in our earlier work, which shows the existence of intrinsic RTFM in nanocrystalline $Zn_{1-x}Co_xO$ particles [17]. In particular, the spectral features between 775 and 785 eV are assigned to the Co 2p3/2–3d5/2 (L3-edge) transitions, and those in the region 790–798 eV to the Co 2p1/2–3d3/2 (L2-edge) transitions. Further it can be observed that, the spectral features L3 and L2-edges are same for all samples of Co doped ZnO and multiple absorptions were observed around L3 and L2-edges, which are broadened with 'Co' concentration and correspondingly the intensities of spectral features increases. Further the investigation of the presence of any Co ion clusters or any oxide phases and the electronic structure is indeed required by means of simulations in

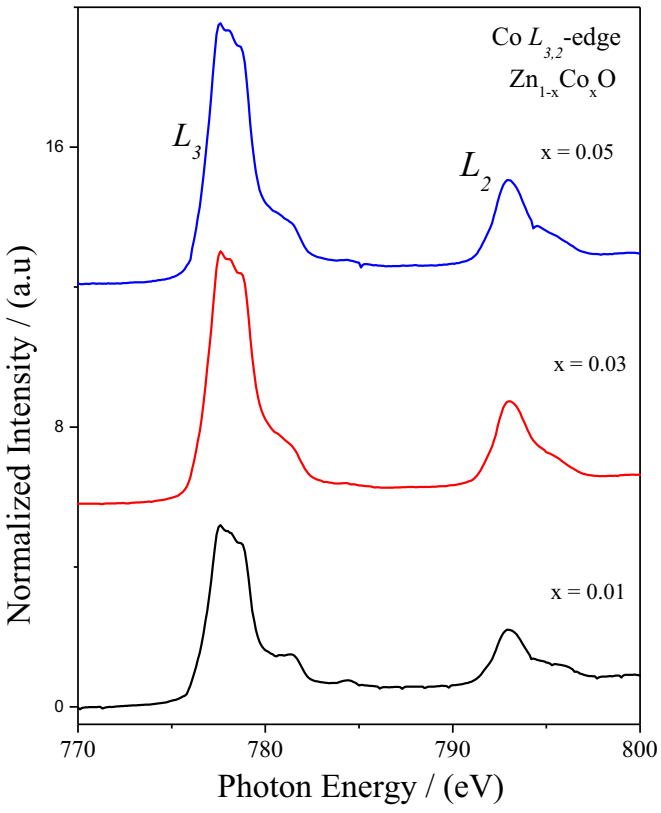

Fig. 3. NEXAFS spectra of $Zn_{1-x}Co_xO$ (x=0, 0.01 and 0.03) taken at Co $L_{3,2}$ edge.

order to understand the local environment of the substituent in the host matrix, that is, the valance state, symmetry and crystal field splitting of Co in the host matrix. Hence to understand the local environment of the 'Co' ions in the host matrix ($Zn_{1-x}Co_xO$), atomic multiplet calculations (simulations) were performed for various symmetries with different crystal field splitting (10Dq) values for all possible valence states of the 'Co' ions at the Co $L_{3,2}$-edge using CTM4XAS software [20]. The calculated (simulated) spectra of 'Co' in 2+ and 3+ valence states with different values of crystal field splitting (10Dq) is depicted in Fig. 4. The results of these calculated spectra with 'Co' in 2+ (Fig. 4(a)–(i)), and 3+ state (Fig. 4(j)–(n)) and for CoO (Fig. 4(o)) are compared with experimentally observed spectra, in particular, compared with the experimental spectra of $Zn_{0.99}Co_{0.01}O$ (Fig. 4(p)) [17]. The crystal field splitting (10Dq) value used to obtain the simulation is shown in respective plot of Fig. 4. From Fig. 4, the negative values of 10Dq correspond to the tetrahedral symmetry, whereas the positive values represent the octahedral symmetry and the zero crystal field value means that the ion is in spherical symmetry. The spectral features were broadened with a Lorentzian and convoluted with Gaussian broadening of 0.2 eV each to simulate the lifetime broadening and to simulate the experimental resolution, respectively in order to compare the spectral features of the atomic multiplet simulations with the experimental spectra. The various parameters used in the above simulations are tabulated in the Table 1. On comparing the experimental spectra with the simulated spectra of Co $L_{3,2}$ edge, the experimentally observed NEXAFS spectra was found to be in better agreement with the simulated spectra of Co^{2+} in tetrahedral symmetry with $10Dq = -0.6$ eV, in agreement with the reported value [21–22]. Also, it is found from the literature that, various groups have reported different values of 10Dq, for example, −1 eV by Krishnamurthy et al. [23] and −0.7 eV by Kobayashi et al. [24]. We have also given the calculations performed for $10Dq = -0.7$ and −1.0 eV in Fig. 4 and those features were deviating from the experimental spectral features. From our results, it is seen that, the calculations are better reproduced the L_3-edge as compared to the L_2-edge, since L_3-edge is more sensitive to the local environment [25]. It is observed that, the features between 775–785 eV and 790–798 eV

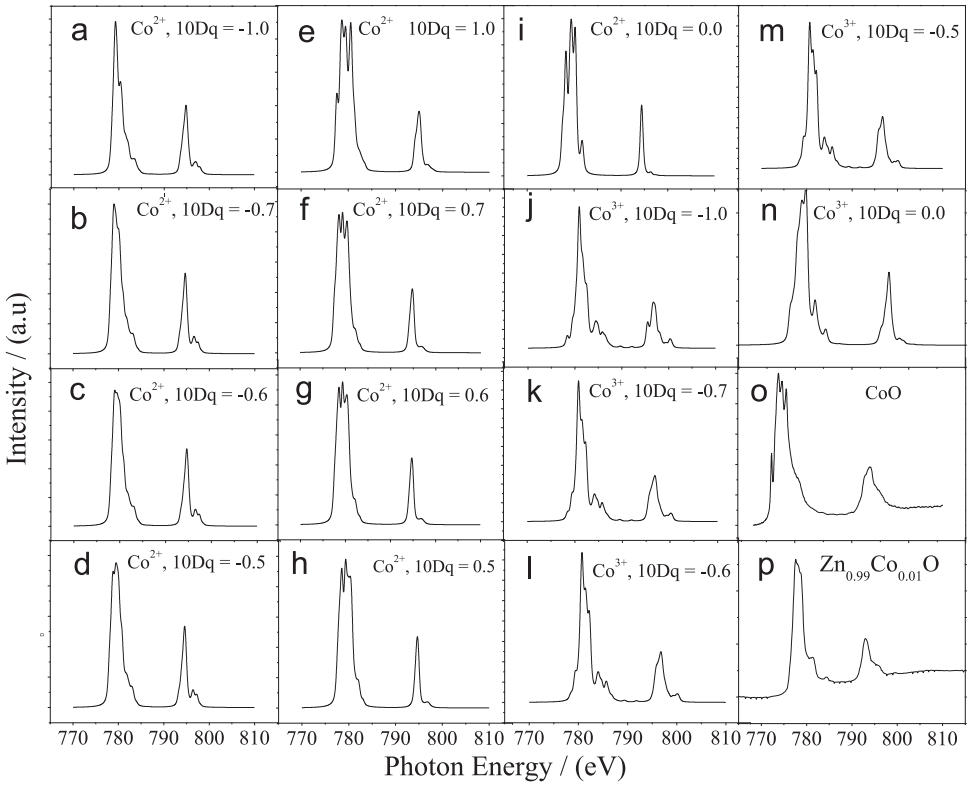

Fig. 4. The $L_{3,2}$ edge calculated using atomic multiplet calculations for various crystal field splitting (10Dq) values.

Table 1
The different parameters used in the atomic multiplet calculations/simulations.

Valence state of Co	Symmetry	10Dq (eV)	Gaussian broadening (eV)	Lorenzian broadening (eV)	Slater integral reduction (%)			SO coupling reduction (%)	
					Fdd	Fpd	Gpd		
Co^{2+}	Tetrahedral	−1.0	0.2	0.2	1.0	1.0	1.0	1.0	1.0
Co^{2+}	symmetry	−0.7							
Co^{2+}		−0.6							
Co^{2+}		−0.5							
Co^{2+}	Spherical symmetry	0.0	0.2	0.2	1.0	1.0	1.0	1.0	1.0
Co^{3+}		0.0							
Co^{2+}	Octahedral symmetry	0.5	0.2	0.2	1.0	1.0	1.0	1.0	1.0
Co^{2+}		0.6							
Co^{2+}		0.7							
Co^{2+}		1.0							
Co^{3+}	Tetrahedral	−1.0	0.2	0.2	1.0	1.0	1.0	1.0	1.0
Co^{3+}	symmetry	−0.7							
Co^{3+}		−0.6							
Co^{3+}		−0.5							

are better reproduced for $10Dq = -0.6$ eV. The other common valence state of Co is 3+, the calculations performed (Fig. 4(j)–(n)) in the tetrahedral symmetry show a large spread as compared to the experimental spectra. We have also compared the experimental spectra with the calculated spectra of CoO, in which the features of L_3 edge are entirely different though L_2 edge features are equivalently coinciding and are also found that, the spectral features entirely different from the other oxide phase [12]. Hence, presence of other oxide (impurity) phases of 'Co' is ruled out, as seen from the XRD results in which no peaks corresponding to any of the cobalt oxide phases were detected. From the above results, on comparison between the experimental and simulated spectra of Co $L_{3,2}$ edge, we conclude that, (i) the 'Co' is substituting at the 'Zn' site in the ZnO matrix without formation of impurities; no cobalt clusters and oxide phases are present in the system, (ii) in $Zn_{1-x}Co_xO$ matrix, 'Co' exist in 2+ valence state and (iii) is tetrahedrally surrounded by four 'O' atoms with crystal field splitting value of −0.6 eV.

3.1. UV–visible spectroscopy

Further to investigate the effect of Co substitution on the optical band gap energy, the optical diffuse reflectance spectra were recorded along with optical absorption spectra using diffuse reflectance spectroscopy and are depicted in Fig. 5. It is observed from Fig. 5(a) that, the absorption edge of $Zn_{1-x}Co_xO$ nanoparticles is red shifted with increasing 'Co' content as compared to the band gap of bulk ZnO (3.37 eV). Also, an increase of absorbance/decrease of reflectance is observed in the visible wavelength region with increase of 'Co' content in the sample. From Fig. 5(a), the spectra show an additional absorption peaks correspond to the transitions related to Co^{2+} levels [11] along with band edge absorption corresponding to ZnO. The absorption observed around 660, 610, and 560 nm in the visible range were correlated with the *d–d* transitions of the tetrahedrally coordinated Co^{2+} ions and attributed, respectively, to $^4A_2(^4F) \rightarrow {}^2E(^2G)$, $^4A_2(^4F) \rightarrow {}^4T_1(^4P)$ and $^4A_2(^4F) \rightarrow {}^4A_1\ (^4G)$ [26–28]. This indicates that the 'Co' ions have substituted the Zn^{2+} ions. This shows the presence of 'Co' in a tetrahedral crystal field in the +2 state supporting our earlier reports [17].

The optical band gap of $Zn_{1-x}Co_xO$ (x=0, 0.01, 0.03, 0.05 and 0.07) are estimated using the diffused reflectance data (Fig. 5(b)). The acquired diffuse reflectance spectrum can be converted to Schuster–Kubelka–Munk function using the formula [29];

$$F(R_\infty) = \frac{(1 - R_\infty)^2}{2R_\infty} = \frac{k}{s} \quad (1)$$

where 'k' is the absorption co-efficient, 's' is the scattering co-efficient and 'R_∞' is the Reflectance.

The vertical axis is converted to quantity $F(R_\infty)$, which is proportional to the absorption co-efficient. Hence, the 'α' in the Tauc equation can be replaced with $F(R_\infty)$. Therefore, for direct allowed transition, Tauc's relation becomes;

$$\left(h\nu F(R_\infty)\right)^2 = A\left(h\nu - E_g\right) \quad (2)$$

Fig. 6 shows the plot of $(h\nu F(R_\infty))^2$ along y-axis vs $h\nu$ along x-axis. The E_g values are determined by extrapolating the linear region of the $(h\nu F(R_\infty))^2$ vs $h\nu$, that is, the $h\nu$ value of x-axis at $(F(R)$

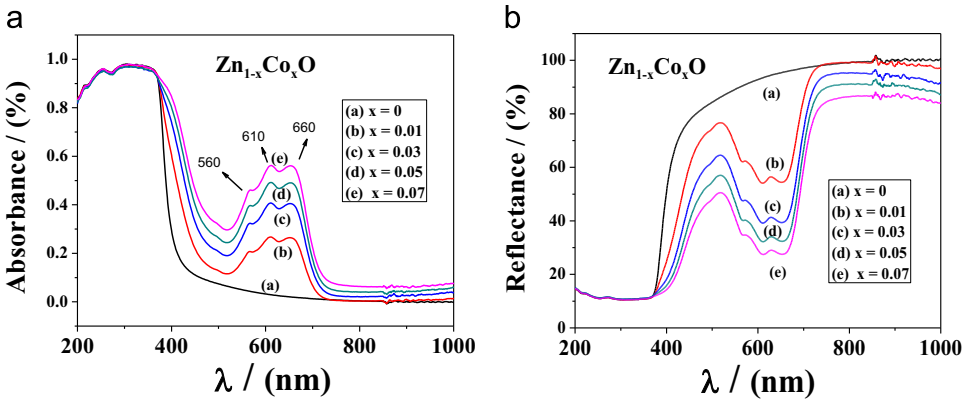

Fig. 5. Diffuse (a) absorbance and (b) reflectance spectra of $Zn_{1-x}Co_xO$ samples.

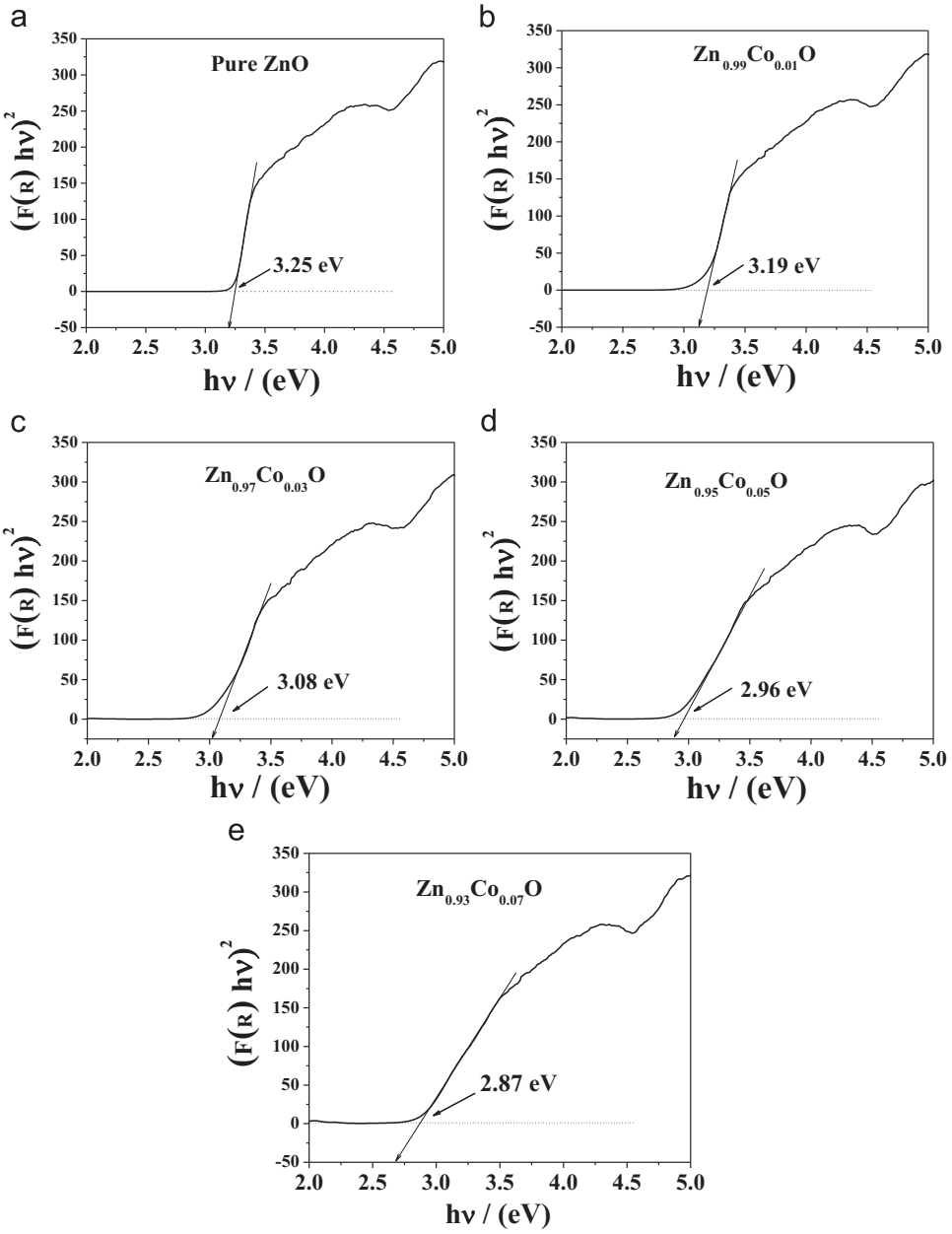

Fig. 6. $(h\nu F(R_\infty))^2 - h\nu$ curves for $Zn_{1-x}Co_xO$ ($x=0$, 0.01, 0.03, 0.05 and 0.07) samples.

$h\nu)^2=0$ gives the band gap (E_g).

The estimated band gap of $Zn_{1-x}Co_xO$ ($x=0$, 0.01, 0.03, 0.05 and 0.07) samples are 3.25 eV, 3.19 eV, 3.08 eV, 2.96 eV and 2.87 eV, respectively. The band gap of Co doped ZnO shows a decrease with increasing Co concentration (Fig. 6), similar to the earlier observations [14–15]. This large red shift could be attributed to the modification of the band structure due to the substitution of Co^{2+} at Zn^{2+} which was reported to show a band-gap narrowing effect, as reported by Kim et al. [14] and Bouloudenine et al. [15]. That is, the band gap of Co doped ZnO samples decreases with increase of Co concentration in ZnO. It is also reported in the literature [12] that, the band gap of Co doped ZnO increases with increase in Co concentration and this blue shift was explained on the basis of Moss–Burstein effect [13]. Whereas in our samples opposite trend was observed. Hence further explanation is required to understand the fact.

Further, in order to explain the band gap narrowing effect, many groups have suggested that, the alloying effect of parent compound with some impurity phases may be responsible for the band gap narrowing effect [30]. On one hand, the alloying effect from ZnO to CoO/Co_3O_4 can be neglected because the band gap decreases below the band gap energy of CoO (3.0 eV) [31] and is higher than that of Co_3O_4 (2.07 eV) [32]. On the other hand, no phase of CoO/Co_3O_4 have been detected from the above XRD measurements and NEXAFS spectra [17]. So the other possibility is the formation of $Zn_{1-x}Co_xO$ phases in Co doped ZnO than in pure ZnO. Therefore the Co^{2+} substitution at Zn^{2+} site in $Zn_{1-x}Co_xO$ may be responsible for the band gap narrowing effect [30]. This may be due to the formation of Co related sub-bands in the band gap, and further these sub-bands merg with the conduction band to form a continuous band. Also the observed decrease of E_g from 3.25 to 2.87 eV with increasing Co content from $x=0$ to $x=0.07$ is attributed due to the *sp–d* exchange interactions between the band electrons in ZnO and the localized *d* electrons of the Co^{2+} [27].

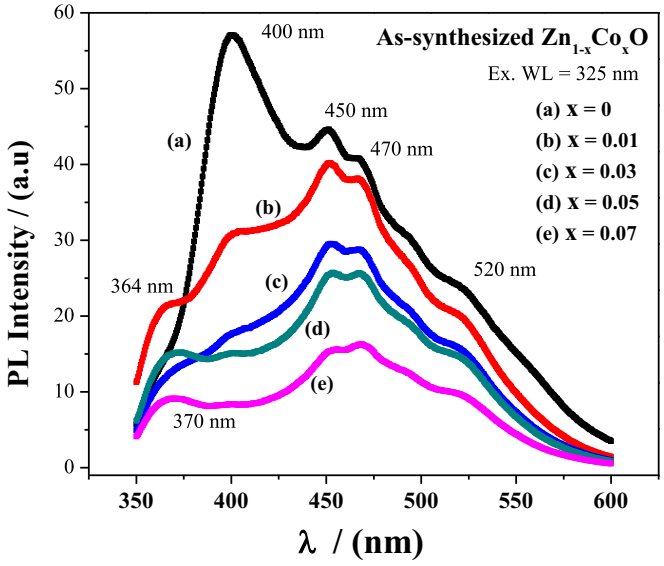

Fig. 7. Photoluminescence spectra of $Zn_{1-x}Co_xO$ (x=0, 0.01, 0.03, 0.05 and 0.07) samples under the excitation wavelength of 325 nm.

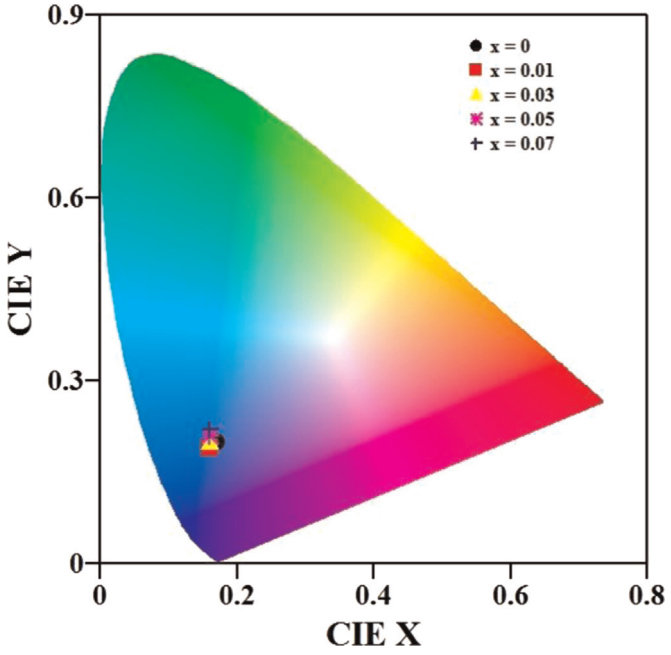

Fig. 8. The CIE chromaticity diagram of $Zn_{1-x}Co_xO$ samples with the calculated color coordinates under the excitation of 325 nm (For interpretation of the references to color in this figure legend, the reader is referred to the web version of this article.).

3.2. Photoluminescence spectroscopy

The PL spectrum is depicted in Fig. 7. As seen from Fig. 7, in case of pure ZnO, a prominent peak around 400 nm, clear and distinct peaks around 450 nm and 470 nm were observed along with a small, considerable shoulder around ~520 nm. The more intense peak at 400 nm (UV-region) is due to near band edge emission (NBE) of the wide band gap ZnO corresponding to the exciton related transition from the localized level below the conduction band to the valence band. Further it is observed that, the intensities of these peaks decrease with increase of 'Co' concentration. In particular the intensity of peak around 400 nm (NBE) reduces abruptly with increase of 'Co' concentration compared to other peaks. Apart from these peaks, a pre-edge peak correspond to ultraviolet (UV) emission around 360–370 nm is observed with increase of 'Co' concentration, is attributed to the near band gap emission [33]. The peaks around 450 nm and 470 nm are corresponding to the blue emissions associated with localized levels in the band gap. These peaks can be attributed to the valence band transitions from intrinsic defects such as 'O' or 'Zn' [34,35], which are created during the synthesis of material. The decrease of their intensity with 'Co' substitution could be due to the increase of non-stoichiometric ZnO content. The small, considerable shoulder peak around 520 nm was attributed to the recombination of electrons with holes trapped in singly ionized oxygen vacancies [36,37] and is observed that, the intensity decreases with Co concentration indicating the decrease of oxygen vacancies. Further, the decrease of peak intensity around 400 nm in Co doped ZnO was attributed to the non-radiative recombination process due to the multiple phonon or lattice vibrations [34,38].

The 1931 CIE chromaticity diagram of the $Zn_{1-x}Co_xO$ samples with various 'Co' concentrations under 325 nm excitations is shown in Fig. 8. The calculated color coordinates for $Zn_{1-x}Co_xO$ (x=0, 0.01, 0.03, 0.05 and 0.07) samples are (0.170, 0.200), (0.160, 0.190), (0.160, 0.200), (0.160, 0.210) and (0.160, 0.220) respectively. From Fig. 8, the calculated color coordinates demonstrate that the emission is in the blue area.

4. Conclusions

In the present investigation, $Zn_{1-x}Co_xO$ (x=0, 0.01, 0.03, 0.05 and 0.07) nanocrystalline particles were synthesized by SCT using L-Valine as a fuel. The detailed studies were carried out to understand the structure, microstructure, electronic structure and magnetic nature of as-synthesized samples. The Rietveld refined XRD patterns reveals the formation of single-phase and absence of secondary phases of 'Co' metal or 'Co' oxides in ZnO wurtzite crystal structure. Formation of nano-sized particles was confirmed through TEM micrographs, in agreement with the crystallite size values obtained from XRD. Also, the lattice parameters estimated using TEM-SAED patterns are in agreement with the Rietveld refinement of XRD data. The electronic structure was determined through the atomic multiplet calculations/simulations performed at Co $L_{3,2}$ edge to determine the valance state, symmetry and crystal field splitting. The spectral features of the experimentally observed NEXAFS spectra is in better agreement with the simulated spectra of Co^{2+} in tetrahedral symmetry with $10Dq = -0.6$ eV and the spectral features of $Zn_{1-x}Co_xO$ are entirely different from those related to Co metal and other oxide phases, which rules out the presence of impurity phases and Co clusters. The diffused reflectance results shows that, the band gap energy, E_g decreases with increase in Co content in ZnO. This Red shift of band gap (E_g) was observed due to the possibility of the formation of $Zn_{1-x}Co_xO$ phases in Co doped ZnO than in pure ZnO. Therefore the Co^{2+} substitution at Zn^{2+} site in $Zn_{1-x}Co_xO$ may be responsible for the band gap narrowing effect and also it was attributed due to the *sp–d* exchange interactions between the band electrons in ZnO and the localized *d* electrons of the Co^{2+}. Also, 'Co' induced defect formation in as-synthesized materials were studied using PL. It was observed that, an enhancement of a prominent pre-edge peak corresponds to ultraviolet (UV) emission around 360–370 nm with Co concentration along with near band edge emission (NBE), where as other observed features reduce due to the increase of non-stoichiometric ZnO content. CIE chromaticity diagram shows that, all the samples show emission in blue region. Hence, the samples could be the potential candidates for the blue light emitting devices.

Acknowledgments

Authors (S.N. and B.A.) are grateful to UGC-DAE-CSR, Kalpakkam Node for the financial support through CRS no. CSR-KN/CRS-22. Authors thank Dr. S. Amrithapandian, UGC-DAE-CSR/IGCAR, Kalpakkam for TEM measurements. Authors also thank Nishad G Deshpande, Y.C. Shao, Way-Faung Pong, Tamkang University and National Synchrotron Radiation Research Center (NSRRC), Taiwan for providing beamline to carry out NEXAFS measurements.

References

[1] D.B. Laks, Chris G. Van de Walle, G.F. Neumark, Sokrates T. Pantelides, Appl. Phys. Lett. 63 (10) (1993) 1375.
[2] J. Pearton, D.P. Norton, K. Ip, Y.W. Heo, T. Steiner, Superlattices Microstruct. 34 (2003) 3–32.
[3] H. Ohno, Science 281 (1998) 951.
[4] T. Dietl, H. Ohno, F. Matsukura, J. Cibert, D. Ferrand, Science 287 (2000) 1019.
[5] K. Sato, H. Katayama-Yoshida, Jpn. J. Appl. Phys. 39 (2000) L555.
[6] K.C. Patil, M.S. Hedge, Tanu Rattan, S.T. Aruna, Chemistry of Nanocrystalline Oxide Materials: Combustion Synthesis, Properties and Applications, Properties and Applications, World Scientific, Singapore, 2008.
[7] P.K. Sharma, R.K. Dutta, A.C. Pandey, S. Layek, H.C. Verma, J. Magn. Magn. Mater. 321 (2009) 2587–2591.
[8] B. Angadi, Y.S. Jung, W.K. Choi, R. Kumar, K. Jeong, S.W. Shin, J.H. Lee, J.H. Song, M. Wasi Khan, J.P. Srivastava, Appl. Phys. Lett. 88 (2006) 142502.
[9] R. Kumar, F. Singh, B. Angadi, J.W. Choi, W.K. Choi, K. Jeong, J.H. Song, M. Wasi Khan, J.P. Srivastava, R.P. Tandon, J. Appl. Phys. 100 (2006) 113708.
[10] R. Kumar, A.P. Singh, P. Thakur, K.H. Che, W.K. Choi, B. Angadi, S.D. Kaushik, S. Patnaik, J. Phys. D 41 (2008) 155002.
[11] S. Venkataprasad Bhat, F.L. Deepak, Solid State Commun. 135 (2005) 345–347.
[12] S.A. Ansari, A. Nisar, B. Fatma, W. Khan, A.H. Naqvi, Mater. Sci. Eng. B 177 (2012) 428–435.
[13] S. Suwanboon, T. Ratana, W.T. Ratana, Walailak J. Sci. Technol. 4 (1) (2007) 111.
[14] K.J. Kim, Y.R. Park, Appl. Phys. Lett. 81 (2002) 1420.
[15] M. Boulouddeine, N. Viart, S. Colis, A. Dinia, Chem. Phys. Lett. 397 (2004) 73.
[16] FullProf, '⟨http://www.ill.eu/sites/fullprof/php/downloads.html⟩'. (accessed 07.02.15).
[17] S. N, B. Angadi, K.G.M. Nair, N.G. Deshpande, Y.C. Shao, W.-F. Pong, J. Electron. Spectrosc. Rel. Phenom. 195 (2014) 179–184.
[18] G.K. Williamson, W.H. Hall, Acta Metall. 1 (1953) 22–31.
[19] Unit Cell, 'http: //www.ccp14.ac.uk/ccp/web-mirrors/crush/astaff/holland/UnitCell.html' (accessed 07.02.15).
[20] E. Stavitski, F.M.F. de Groot, Micron 41 (2010) 687.
[21] A.P. Singh, R. Kumar, P. Thakur, N.B. Brookes, K.H. Chae, W.K. Choi, J. Phys.: Condens. Matter 21 (2009) 185005.
[22] S.C. Wi, J.-S. Kang, J.H. Kim, S.-B. Cho, B.J. Kim, S. Yoon, B.J. Suh, S.W. Han, K. H. Kim, K.J. Kim, B.S. Kim, H.J. Song, H.J. Shin, J.H. Shim, B.I. Min, Appl. Phys. Lett. 84 (2004) 4233.
[23] S. Krishnamurthy, C. McGuinness, L.S. Dorneles, M. Venkatesan, J.M.D. Coey, J. G. Lunney, C.H. Patterson, K.E. Smith, T. Learmonth, P.-A. Glans, T. Schmitt, J.-H. Guo, J. Appl. Phys. 99 (2006) 08M111.
[24] M. Kobayashi, Y. Ishida, J. I Hwang, T. Mizokawa, A. Fujimori, K. Mamiya, J. Okamoto, Y. Takeda, T. Okane, Y. Saitoh, Y. Muramatsu, A. Tanaka, H. Saeki, H. Tabata, T. Kawai, Phys. Rev. B 72 (2005) 201201 (R).
[25] F.M.F. de Groot, M. Abbate, J. van Elp, G.A. Sawatzky, Y.J. Ma, C.T. Chen, F. Sette, J. Phys.: Condens. Matter 5 (1993) 2277.
[26] S. Ramachandran, Ashutosh Tiwari, J. Narayan, Appl. Phys. Lett. 84 (2004) 25.
[27] Xue-Chao Liu, Er-Wei Shi, Zhi-Zhan Chen, Hua-Wei Zhang, Li-Xin Song, Huan Wang, Shu-De Yao, J. Cryst. Growth 296 (2006) 135–140.
[28] P. Koidl, Phys. Rev. B 15 (1977) 2493.
[29] B.J. Wood, R.G.J. Strens, Mineral. Mag. 43 (1979) 509–518.
[30] Arham S. Ahmed, Shafeeq M. Muhamed, M.L. Singla, Sartaj Tabassum, Alim H. Naqvi, Ameer Azam, J. Lumin. 131 (2011) 1–6.
[31] V.I. Anisimov, M.A. Korotin, E.Z. Kurmaev, J. Phys.: Condens. Matter 2 (1990) 3973.
[32] Mingce Long, Weimin Cai, Jun Cai, Baoxue Zhou, Xinye Chai, Yahui Wu, J. Phys. Chem. B 110 (2006) 20211–20216.
[33] Y.C. Kong., D.P. Yu, B. Zhang., W. Fang, S.Q. Feng, Appl. Phys. Lett. 78 (2001) 407.
[34] R. Bhargava, P.K. Sharma, R.K. Dutta, S. Kumar, A.C. Pandey, N. Kumar, Mater. Chem. Phys. 120 (2010) 393–398.
[35] Shahid Husain, Lila A. Alkhtaby, Irshad bhat, Emilia Giorgetti, Angela Zoppi, Maurizio Muniz Mirand, J. Lumin. 154 (2014) 430–436.
[36] K. Vanheusden, W.L. Warren, C.H. Seager, D.R. Tallant., J.A. Voigt, B.E. Gnade, Appl. Phys. Lett. 79 (1996) 7983.
[37] P.K. Sharma, R.K. Dutta, A.C. Pandey, J. Colloid Interface Sci. 345 (2010) 149–153.
[38] P.V. Radovanovic, C.J. Barrlet, S. Gradecak, F. Qian, C.M. Lieber, Nano. Lett. 5 (2005) 1407.